

Topological phases in interacting spin-1 systemsA. Alnor¹, T. Bækkegaard^{1,2} and N. T. Zinner^{1,3}¹*Department of Physics and Astronomy, Aarhus University, DK-8000 Aarhus C, Denmark*²*Institute of Photonics, Leibniz University Hannover, Nienburgerstr. 17, 30519 Hannover*³*Aarhus Institute of Advanced Studies, Aarhus University, DK-8000 Aarhus C, Denmark* (Received 23 October 2021; revised 24 July 2022; accepted 28 September 2022; published 7 November 2022)

Different topological phases of quantum systems have become areas of increased focus in recent decades. In particular, the question of how to realize and manipulate systems with a nontrivial first Chern number is pursued both experimentally and theoretically. Here we go beyond typical spin-1/2 systems and consider both single and coupled spin-1 systems as a means of realizing higher first Chern numbers and studying the emergence of different topological phases. We show that rich topological phase diagrams can be realized by coupling two spin-1 systems using both numerical and analytical methods. Furthermore, we consider a concrete realization of spin-1 systems using a superconducting circuit. This realization includes nonstandard spin-spin interaction terms that may endanger the topological properties. We argue, however, that the realistic circuit Hamiltonian including all terms should be expected to show the rich phase structure as well. This puts our theoretical predictions within reach of state-of-the-art experimental setups.

DOI: [10.1103/PhysRevB.106.174505](https://doi.org/10.1103/PhysRevB.106.174505)**I. INTRODUCTION**

The phenomena of topological properties of quantum systems have seen much research in recent years as a tool for describing global nontrivial features. Derived in 1950 by T. Kato [1], though named after M. V. Berry, who discovered it independently in 1984 [2], the Berry phase, also called the geometric phase, arises by adiabatically varying the parameters governing the quantum system. This gives rise to the Berry curvature, whose closed two-dimensional (2D) surface integral is an integer multiple of 2π . This integer is the first Chern number of the system, a topological invariant [3–7]. This connection between varying external parameters and global features of the system gives a method of experimentally probing the topological features of quantum systems [8,9]. Two regions in the space of external parameters with differing ground-state topological properties, i.e., differing topological quantum numbers, are considered as distinct topological phases [10]. These topological phases are considered as quite stable since the transitions between the two can only happen by closing the energy gap between the ground state and the first excited state. These distinct topological phases and the dependence on externally changing parameters will be the focus of our attention.

Topological properties of quantum systems are of increasing interest in condensed matter physics, due to exhibiting interesting properties that are typically not seen in classical systems. Some of these properties are believed to have technological applications, including their use in quantum information technology, topological insulators, and unconventional superconductors [11–13]. For instance, for two-dimensional filled bands and three-dimensional Fermi surfaces, the Hall conductance of the system is characterized by the Chern number [13].

Due to the difficulty of probing topological properties in physical systems directly, emulation of the systems by other means is sometimes employed. In 1982, Richard Feynman proposed to use quantum simulation to investigate otherwise inaccessible quantum phenomena [14]. In recent years, there have been extended efforts to perform quantum simulation [15] of systems that exhibit nontrivial Chern numbers using several different platforms including cold atomic gases [16,17], Rydberg systems [18,19], trapped ions [20,21], and photonics [22,23]. Here we will focus on the platform of superconducting circuits [24–28] as our main platform for studying systems that may realize nontrivial first Chern numbers. Inspired by two papers from 2014 [29,30], in which the Chern number was experimentally measured in artificial spin-1/2 qubit systems of quantum circuits, we will consider here how higher spins can realize topological phases. In particular, we will study spin-1 systems, also known as qutrits. These have been the focus of attention for more than a decade within the realm of superconducting circuits [31–39].

Here we explore how to obtain nontrivial Chern numbers in spin systems realized as a quantum simulation in the sense that they do not represent real particles, but rather achieve the same dynamics using superconducting circuits. We will explore topological phases in three types of spin-1 systems. First, we will look at a simple spin-1 system controlled by a magnetic field. Second, we will consider a system with two coupled qutrit subsystems controlled by a single coupling parameter. Finally, we will look at an example of how this could be implemented in a system of qutrits using superconducting circuits that was suggested in a recent paper [40,41] using three different coupling parameters. The analysis will be based on both analytic solutions and numerical simulation using the QUTIP simulation package [42]. Comments are placed throughout on the aspects of superconducting circuits

that might be relevant for physical realization. The exposition below will start by consider the systems as abstract theoretical models and then we proceed to discuss the concrete setups within superconducting circuits.

II. FORMALISM

In this section we introduce the basic theoretical framework and explain our notation. We will make use of spin operators. These will be denoted S^i for $i = x, y, z, +, -$. The spin vector is defined as $\mathbf{S} = (S^x, S^y, S^z)$. In the case of an operator S working on a particular system j , we will use the notation S_j . As an example, the z component of the spin for the first particle is S_1^z . When dealing with spin-1 three-level systems, the states will be given in the basis $\{\uparrow, 0, \downarrow\}$ and the systems will be referred to as qutrits.

A. Brief introduction to Berry's phase and related concepts

The derivation of Berry's phase, and of the related Chern number, can be found many places in literature (see, for example, Chap. 2 of Ref. [13] or Chap. 5 of Ref. [43]). We will simply state the main results.

Adiabatic time evolution is defined as time evolution where the parameters of the system are changed slowly, allowing the system to adapt to the change. The adiabatic theorem loosely states that in the adiabatic limit, a system initially being in the n th eigenstate will be in the n th eigenstate of the new system. If one considers situations where the parameters of the Hamiltonian will be changed slowly and return to the initial ones, one might expect that the system will then be identical to the original system, however, a phase may be picked up.

If a system starts out in the eigenstate $|n\rangle$ of $H(0)$, then it remains in the eigenstate $|n\rangle$ of $H(t)$, and the total state can be written as

$$|\Psi(t)\rangle = e^{i\gamma_n(t)} e^{i\theta_n(t)} |n(t)\rangle, \quad (1)$$

where

$$\gamma_n(t) = \int_0^t \langle n(t') | \frac{\partial}{\partial t'} | n(t') \rangle dt' \quad (2)$$

is Berry's phase and θ_n is the dynamic phase, which is not of interest here.

B. Degeneracies and Chern numbers

We let \mathbf{R} be a vector in the parameter space, i.e., the components that control the Hamiltonian are collected in this vector. The Berry phase gives rise to the Berry curvature \mathbf{F}_n , a local (in \mathbf{R} -space) property of the quantum system, which in the three-dimensional case can be calculated as

$$\mathbf{F}_n(\mathbf{R}) = -\text{Im} \sum_{m \neq n} \frac{\langle n | \nabla_{\mathbf{R}} H | m \rangle \times \langle m | \nabla_{\mathbf{R}} H | n \rangle}{(E_m - E_n)^2}. \quad (3)$$

$$S^x = \frac{\hbar}{\sqrt{2}} \begin{pmatrix} 0 & 1 & 0 \\ 1 & 0 & 1 \\ 0 & 1 & 0 \end{pmatrix}, \quad S^y = \frac{i\hbar}{\sqrt{2}} \begin{pmatrix} 0 & -1 & 0 \\ 1 & 0 & -1 \\ 0 & 1 & 0 \end{pmatrix}, \quad S^z = \hbar \begin{pmatrix} 1 & 0 & 0 \\ 0 & 0 & 0 \\ 0 & 0 & -1 \end{pmatrix}, \quad \text{and } S^+ = \hbar\sqrt{2} \begin{pmatrix} 0 & 1 & 0 \\ 0 & 0 & 1 \\ 0 & 0 & 0 \end{pmatrix} = (S^-)^\dagger \quad (6)$$

from this point on, where units in which $\hbar = 1$ are used.

As can be seen from Eq. (3), degeneracies are the source of Berry curvature due to the divergence that will result from them.

The integral of the Berry curvature over a closed surface is quantized in integer multiples of 2π [44], and the integer is the first Chern number of the system,

$$\text{Ch}_1 = \frac{1}{2\pi} \oint_{\mathcal{S}} \mathbf{F} \cdot d\mathbf{S}, \quad (4)$$

where \mathbf{S} is the normal vector of the surface \mathcal{S} spanned by the closed loop in parameter space. The first Chern number is often simply called *the* Chern number and will be referred to as such throughout this text. The Chern number is a topological invariant. In this case, it reveals the number of enclosed degeneracies.

The Berry curvature is sometimes described as an effective magnetic field with degeneracies acting as the source of the field, equivalent to magnetic monopoles (see, for instance, Ref. [45]). In this framework, the Chern number is simply found using Gauss' law [46] and the number is signaling the enclosed degeneracies with their monopole charge. In a similar vein, Gritsev *et al.* showed that the Berry curvature produces an effective force [47] in a system initially in the ground state driven by a slow linear parameter change. By changing the parameters in the μ direction with rate $v_\mu = \partial\mu/\partial t$, the system, with time dependent wave function $|\Psi(t)\rangle$, experiences a generalized force in the ν direction $M_\nu = -\partial H/\partial v$, related to the $\mu\nu$ component of the Berry curvature,

$$\langle M_\nu(t) \rangle = \langle \Psi(t) | M_\nu | \Psi(t) \rangle = \langle 0 | M_\nu | 0 \rangle + v_\mu F_{0,\mu\nu} + \mathcal{O}(v_\mu^2), \quad (5)$$

where $\mathcal{O}(v_\mu^2)$ are higher-order terms that will be neglected due to the change happening slowly. The first term is the value in the adiabatic limit $v_\mu = 0$ in which case the system stays in the exact ground state at all times. Thus, we can directly measure the Berry curvature from the linear response by measuring $\langle M_\nu \rangle$. Both prescriptions of the curvature are used throughout this paper, Eq. (3) when making analytical predictions and Eq. (5) when performing simulations.

III. THREE-LEVEL SYSTEMS

As a warm-up to the coupled systems and an introduction to how we treat the system analytically, we start by considering a relatively generic spin-1, or three-level, system. We follow previous discussions of similar systems with spin 1/2 [29,30], as well as the study of Ref. [36] where topological band structure was investigated with a superconducting circuit and the measurement of a Chern number greater than unity was achieved.

The spin matrices for spin 1 will be taken to be of the form

A. Simple three-level system

We first take a purely analytical approach to the simple three-level system. This procedure is identical to the one performed by Berry in Ref. [2]. The Hamiltonian we will be dealing with is that of a spin 1 in a magnetic field, and has the form

$$H = \mathbf{R} \cdot \mathbf{S}, \quad (7)$$

where \mathbf{R} is the vector in parameter space. The Berry curvature is calculated using Eq. (3). Explicitly calculating its eigenvalues, we see that it has energies $E_{\uparrow} = -E_{\downarrow} = |\mathbf{R}| = R$ and $E_0 = 0$. A quick calculation gives $(E_{\uparrow/\downarrow} - E_{\downarrow/\uparrow})^2 = 4R^2$ and $(E_{\uparrow/\downarrow} - E_0)^2 = (E_0 - E_{\uparrow/\downarrow})^2 = R^2$, while $\nabla_{\mathbf{R}}H = \mathbf{S}$. Since the Hamiltonian is spherically symmetric, we can fix \mathbf{R} to point in the \hat{z} direction. We can then write \mathbf{S} as

$$\mathbf{S} = \frac{1}{2}(S^+ + S^-)\hat{x} + \frac{1}{2i}(S^+ - S^-)\hat{y} + S_z\hat{z}. \quad (8)$$

Explicit calculation of the Berry curvature by Eq. (3) yields, by invoking the requirement for spin eigenvalues and applying orthogonality,

$$\mathbf{F}_{\uparrow} = -\frac{\hat{z}}{R^2}. \quad (9)$$

Remembering that we had rotated our axes to point in the \hat{z} direction, we arrive at the expression

$$\mathbf{F}_{\uparrow} = -\frac{\hat{\mathbf{R}}}{R^2}, \quad (10)$$

while similar calculation will result in

$$\mathbf{F}_{\downarrow} = \frac{\hat{\mathbf{R}}}{R^2}, \quad \mathbf{F}_0 = \mathbf{0}. \quad (11)$$

The integral of $\mathbf{F}_{\uparrow/\downarrow}$ is well known in electrodynamics [46], and the integral over any surface enclosing $\mathbf{0}$ will yield

$$\oint_S \mathbf{F}_{\uparrow} \cdot d\mathbf{a} = -4\pi. \quad (12)$$

So, up to a sign, we arrive at $\text{Ch}_1 = 2$ when the degeneracy is enclosed. This degeneracy is known as the Weyl point and in this case has topological charge 2.

1. Simulating the simple system

In order to address the potential conditions of an experiment with a three-level system, we now simulate a protocol for measuring the Chern number by use of Eq. (5). We consider Hamiltonians of the form

$$H = -(H_0 S^z + \mathbf{H}_r \cdot \mathbf{S}), \quad (13)$$

with $\mathbf{H}_r = (H^x, H^y, H^z) = H_r[\sin(\theta)\cos(\phi), \sin(\theta)\sin(\phi), \cos(\theta)]$. For all simulations we use Hamiltonian parameters that are within the usual set of values for superconducting circuits [48–50], and we set $H_r = 10 \times 2\pi$ MHz. The system is initialized in its instantaneous ground state for a particular value of H_0 . We then change (ramp) the value of θ from 0 to π as $\theta(t) = \pi t/t_{\text{ramp}}$, finally stopping at $t = t_{\text{ramp}}$. We denote

$$v_{\theta} = \frac{\partial \theta}{\partial t}. \quad (14)$$

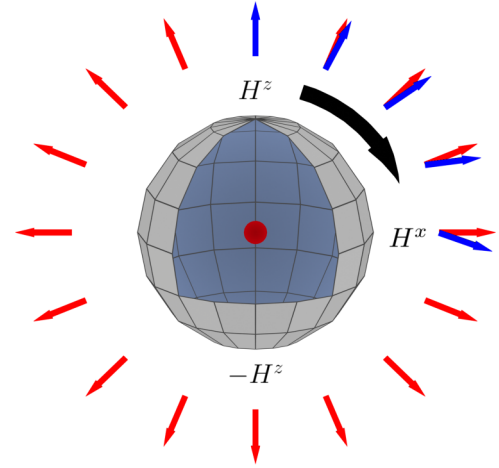


FIG. 1. Schematic of the path traversed in the parameter space over the closed spherical manifold described by \mathbf{H}_r , starting at $\mathbf{H}_r(t=0) = H^z\hat{z}$ and moving in a semicircle to $\mathbf{H}_r(t=t_{\text{ramp}}) = -H^z\hat{z}$. The adiabatic case is represented by red arrows and the measured deflection, caused by the ramping, is represented by blue arrows. Inside the sphere lies the Weyl point causing the deflection from adiabaticity, which is used to extract the Chern number. This figure is based on Fig. 1 in Ref. [30].

By ramping θ like so, we create a curve through parameter space in the shape of a semicircle from $H_r S^z$ to $-H_r S^z$ (see Fig. 1).

Our Hamiltonian is cylindrically symmetric around the z axis and as such, the Berry curvature is independent of ϕ . We therefore fix $\phi(t) = 0$ throughout. The expectation value of the generalized force of the system is then

$$\langle M_{\phi} \rangle = -\left\langle \frac{\partial H}{\partial \phi} \right\rangle = H_r \langle S^y \rangle \sin(\theta). \quad (15)$$

The generalized force for a spin in a magnetic field is zero in the adiabatic limit, as the spin will simply align with the field. As such, the Berry curvature can be found as the leading order correction with Eq. (5). We obtain that the Berry curvature can be calculated as

$$F_{\theta\phi} = F_{\theta 0} = \frac{H_r}{v_{\theta}} \sin(\theta) \langle S^y \rangle. \quad (16)$$

The Chern number is found by integrating the Berry curvature over the entire manifold. However, since the Hamiltonian is cylindrically symmetric, we need only integrate over θ . The Chern number can then be found as

$$\text{Ch}_1 = \frac{1}{2\pi} \int_0^{\pi} \int_0^{2\pi} F_{\theta\phi} d\phi d\theta = \int_0^{\pi} F_{\theta\phi} d\theta. \quad (17)$$

In a physical experiment, θ would be ramped linearly for a time between 0 and t_{ramp} , then $\langle S^y \rangle$ would be measured and the experiment would be performed again, ramping to a different time, so that the evolution can be tracked.

Equation (17) gives a prescription of the Chern number in terms of the Berry curvature. However, since the number is a description of the number of enclosed degeneracies in parameter space, we can also find these analytically. The path described previously is on the surface of a spherical manifold of radius H_r . Thus, in the simple case described here, the

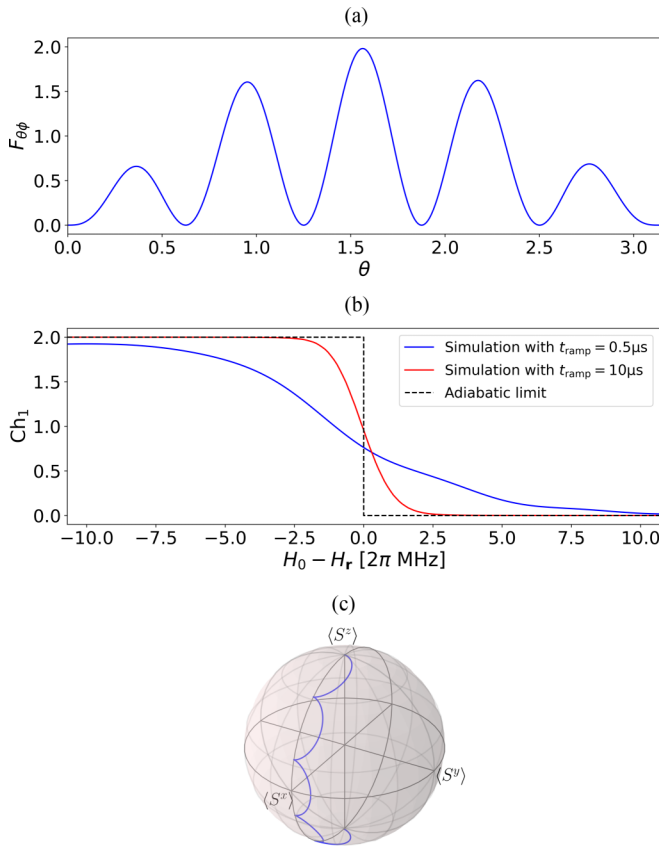


FIG. 2. (a) Plot of the Berry curvature $F_{\theta\phi}(\theta)$ for the case $H_0 = 0$ with $t_{\text{ramp}} = 0.5 \mu\text{s}$ and $H_r = 10 \times 2\pi$ MHz. The integral of $F_{\theta\phi}$ is used to find Ch_1 . (b) Ch_1 for various values of H_0 , with $t_{\text{ramp}} = 0.5 \mu\text{s}$ and $10 \mu\text{s}$. A topological transition occurs when $H_0 = H_r = 10 \times 2\pi$ MHz, where the Weyl point is at the boundary of the ground state manifold. The probing of the topological transition is made clearer in the second case due to the slow ramping. (c) The trajectory of the state on the surface of a sphere spanned by $\langle S^x \rangle$, $\langle S^y \rangle$, and $\langle S^z \rangle$ with $t_{\text{ramp}} = 0.5 \mu\text{s}$, starting from $\langle S^z \rangle = 1$ at $t = 0$ to $\langle S^z \rangle = -1$ at $t = t_{\text{ramp}}$. The deviation from the meridian is used to extract the Berry curvature and the Chern number.

Weyl point lies inside the sphere for $H_0 < H_r$ and outside for $H_0 > H_r$. Comparing with Eq. (12), we see that the Chern number is $\text{Ch}_1 = 2$ when $H_0 < H_r$. Simulating the ramping of θ and integrating $\langle F_{\theta\phi} \rangle$ over the resulting semicircle yields a numerical way to calculate Ch_1 .

For the sake of example, the ramping of θ is performed with $t_{\text{ramp}} = 0.5 \mu\text{s}$. For $H_0 = 0$ this results in the $F_{\theta\phi}$ plotted in Fig. 2(a). In this case the integral gives $\text{Ch}_1 \approx 2$, since the Weyl point is enclosed. The topological nature of the number can be investigated by simulating for different values of H_0 . The result of these simulations is shown in blue in Fig. 2(b). While it is clear that Ch_1 changes from 2 to 0, it does so continuously. This is a result of the measurement technique, as a higher-order response from Eq. (5) makes Eq. (16) invalid. If we instead choose to simulate with $t_{\text{ramp}} = 10 \mu\text{s}$, we get a noticeably sharper transition plotted in red in Fig. 2(b). As expected, a transition occurs at the point $H_0 = H_r$, with $\text{Ch}_1 = 2$ when $H_0 < H_r$ and $\text{Ch}_1 = 0$ when $H_0 > H_r$.

The number of oscillations in $F_{\theta\phi}$ is given by H_r/v_θ . As a result of this, choosing a slower ramping speed will result

in a higher number of oscillations, and therefore a higher resolution in time is needed to accurately determine Ch_1 . Since the integral of $F_{\theta\phi}$ over the sphere is independent of t_{ramp} , Eq. (16) also means that $\langle S^y \rangle$ becomes less pronounced, requiring greater precision in its measurement. On the other hand, higher levels in the superconducting circuit spectrum are more unstable [35]. As a result of this, a fast ramp may then mitigate some of the decay noise that might otherwise occur in slow transition protocols. Due to these considerations, we set $H_r = 10$ MHz and $t_{\text{ramp}} = 0.5 \mu\text{s}$ for the remainder of the paper. This is also consistent with the energy scale of the Hamiltonian of superconducting circuit relevance and in the same order as similar experiments [29,30,36].

In the case of a qubit system, the response can be visualized as a trajectory on a Bloch sphere. Since we are dealing with a qutrit, more parameters are necessary to completely describe the state of the system. We can, however, still visualize the relevant parts of the trajectory, described by $\langle S^x \rangle$, $\langle S^y \rangle$, and $\langle S^z \rangle$. This can be considered as a cross section of the entire space. This trajectory with $t_{\text{ramp}} = 0.5 \mu\text{s}$ for the case $H_0 = 0$ is plotted in Fig. 2(c).

IV. COUPLED THREE-LEVEL SYSTEM

A. Introduction to the coupled three-level system

Having discussed the single three-level system, we now continue to the coupled case. The modification we perform is to add an additional qutrit system coupled to the first with a coupling term $g(S_1^x S_2^x + S_1^y S_2^y)$. This is the generalization to higher spins of the coupled spin-1/2 system as, for instance, discussed in Ref. [30]. Here we will explore how the extra levels and the interactions can influence the phase diagram.

We consider Hamiltonians of the form

$$H = -[H_0 S_1^z + \mathbf{H}_1 \cdot \mathbf{S}_1 + \mathbf{H}_2 \cdot \mathbf{S}_2 - g(S_1^x S_2^x + S_1^y S_2^y)], \quad (18)$$

where we will set $\mathbf{H}_1 = \mathbf{H}_2 = \mathbf{H}_r$, again with

$$\mathbf{H}_r = H_r[\sin(\theta) \cos(\phi), \sin(\theta) \sin(\phi), \cos(\theta)],$$

with $H_r = 10 \times 2\pi$ MHz. As before, the system is initialized in its instantaneous ground state for a fixed value of H_0 and g . We ramp $\theta(t)$, this time for both qutrits simultaneously, with both H_0 and g kept constant. Since g is kept constant for each simulation, by taking the ϕ derivative of Eq. (18), we see that the Berry curvature is obtained as the integral over two separate spherical manifolds. Likewise, the system has $U(1)$ invariance along the z axis, meaning that the system for $H(\theta, 0)$ can be mapped to $H(\theta, \phi)$ as

$$H(\theta, \phi) = e^{i\phi(S_1^z + S_2^z)} H(\theta, 0) e^{-i\phi(S_1^z + S_2^z)}. \quad (19)$$

With this in mind, the Chern number is simply found by integrating the Berry curvature for both qutrits,

$$\text{Ch}_1 = \int_0^\pi \frac{H_r}{v_\theta} \sin(\theta) (\langle S_1^y \rangle + \langle S_2^y \rangle) d\theta. \quad (20)$$

In the limiting case of $g = 0$, we expect this to be equivalent to two isolated qutrits, one of which has a transition where Ch_1 changes by 2 when $H_0 = H_r$, while the other is unaffected by the change in H_0 , i.e., we expect $\text{Ch}_1 = 4$ when $H_0 < H_r$ and $\text{Ch}_1 = 2$ when $H_0 > H_r$. When $g \neq 0$, things become more complicated. We expect multiple phases of the

system to be present, with different values of Ch_1 depending on the strength of H_0 and g . The theoretical phase diagram can again be found by considering the position of degeneracies in the parameter space. We expect the total Ch_1 to be no larger than the sum of the individual Ch_1 for each isolated qutrit, since the coupling and offset is kept constant for each ramp. That is, we expect $\text{Ch}_1 \leq 4$, no matter the value of H_0 and g .

$$H = \begin{pmatrix} -H_0 - 2H_r & 0 & 0 & 0 & 0 & 0 & 0 & 0 & 0 \\ 0 & -H_0 - H_r & 0 & g & 0 & 0 & 0 & 0 & 0 \\ 0 & 0 & -H_0 & 0 & g & 0 & 0 & 0 & 0 \\ 0 & g & 0 & -H_r & 0 & 0 & 0 & 0 & 0 \\ 0 & 0 & g & 0 & 0 & 0 & g & 0 & 0 \\ 0 & 0 & 0 & 0 & 0 & H_r & 0 & g & 0 \\ 0 & 0 & 0 & 0 & g & 0 & H_0 & 0 & 0 \\ 0 & 0 & 0 & 0 & 0 & g & 0 & H_0 + H_r & 0 \\ 0 & 0 & 0 & 0 & 0 & 0 & 0 & 0 & H_0 + 2H_r \end{pmatrix}. \quad (21)$$

We will be localizing Weyl points in the parameter space, as we know from Eq. (3) that this is the location in parameter space that causes a nontrivial Berry curvature. The only relevant coordinate of the Weyl points, the z coordinate, will be denoted H_z .

We block-diagonalize the Hamiltonian in the eigenbasis of J_z . As such, we analyze the system in terms of each value of the total spin along z , m_{tot} .

For $m_{\text{tot}} = \pm 2$, we have energies $E_{\uparrow\uparrow} = -H_0 - 2H_r$ and $E_{\downarrow\downarrow} = H_0 + 2H_r$. For $m_{\text{tot}} = \pm 1$ we have the matrices

$$H_{0\uparrow/0\downarrow} = \begin{pmatrix} -H_0 - H_r & g \\ g & -H_r \end{pmatrix}, \quad H_{\downarrow 0/0\downarrow} = \begin{pmatrix} H_r & g \\ g & H_0 + H_r \end{pmatrix}, \quad (22)$$

with energies $\frac{-H_0 - H_r}{2} \pm \frac{\sqrt{H_0^2 + 4g^2}}{2}$ and $\frac{H_0 + H_r}{2} \pm \frac{\sqrt{H_0^2 + 4g^2}}{2}$, respectively. Finally, the $m_{\text{tot}} = 0$ sector looks like

$$H_{\uparrow\downarrow/00/\downarrow\uparrow} = \begin{pmatrix} -H_0 & g & 0 \\ g & 0 & g \\ 0 & g & H_0 \end{pmatrix}, \quad (23)$$

with energies 0 and $\pm\sqrt{H_0^2 + 2g^2}$. Since we have $\nabla_{\mathbf{R}}H = \mathbf{S} = \frac{1}{2}(S^+ + S^-)\hat{\mathbf{x}} + \frac{1}{2i}(S^+ - S^-)\hat{\mathbf{y}} + S_z\hat{\mathbf{z}}$ and since it is an orthogonal basis, Eq. (3) gives that only states that differ in m_{tot} by 1 will be able to contribute to the Berry curvature. That is, degeneracy from states with a difference in spin other than 1 are irrelevant.

Depending on the values of H_0 and g , there will be three different ground states, which can be found to be

$$|g\rangle = \begin{cases} |\uparrow\uparrow\rangle \\ a_1 |\uparrow 0\rangle - a_2 |0 \uparrow\rangle \\ b_1 |00\rangle - b_2 |\uparrow\downarrow\rangle - b_3 |\downarrow\uparrow\rangle \end{cases}, \quad (24)$$

where a_i and b_i are positive constants. In the case $H_0 = 0$, we get in particular $a_1 = a_2 = b_2 = b_3 = 1/\sqrt{2}$ and $b_1 = 1/2$. As such, the ground state Berry curvature will be different in each case.

B. Analytical solution

We first reorient our Hamiltonian to lie in the $\hat{\mathbf{z}}$ direction, so that $\theta = 0$ or $\theta = \pi$. We can analytically locate the Weyl points of the system by considering this situation. For $\theta = 0$, the Hamiltonian, in the basis $\{|\uparrow, 0, \downarrow\rangle \otimes \{|\uparrow, 0, \downarrow\rangle\}$, reduces to

We first consider $\mathbf{F}_{\uparrow\uparrow}$. Here the curvature stems from degeneracies between $m_{\text{tot}} = +2$ and $m_{\text{tot}} = +1$, and the two resulting ground state degeneracies have z components,

$$H_z \in \left\{ -\frac{H_0}{2} \pm \frac{1}{2}\sqrt{H_0^2 + 4g^2} \right\}. \quad (25)$$

We now consider $\mathbf{F}_{\uparrow 0/0\uparrow}$, the curvature from the states with $m_{\text{tot}} = +1$. Here, the relevant degeneracies are between the $m_{\text{tot}} = +1$ sector and both the $m_{\text{tot}} = +2$ and $m_{\text{tot}} = 0$ sectors. The new ground state degeneracies have z components,

$$H_z \in \left\{ -\frac{H_0}{2} \pm \frac{1}{2}\sqrt{H_0^2 + 4g^2} \mp \sqrt{H_0^2 + 2g^2} \right\}. \quad (26)$$

All remaining values of H_z will, up to a sign, be identical to the ones already found. This can also be seen from our previous argument that $\text{Ch}_1 \leq 4$, with four values of H_z having been found. In total, the four relevant locations are

$$H_z \in \left\{ -\frac{H_0}{2} \pm \frac{1}{2}\sqrt{H_0^2 + 4g^2}, \right. \\ \left. -\frac{H_0}{2} \pm \frac{1}{2}\sqrt{H_0^2 + 4g^2} \mp \sqrt{H_0^2 + 2g^2} \right\}. \quad (27)$$

These are the z components of the Weyl points. From this, we can construct a theoretical phase diagram. This is done in Fig. 3(a). As is evident in the figure, six different phases are present, depending on how many $H_z < |H_r|$, i.e., how many of the degeneracies are enclosed within the sphere.

C. Simulated solution

As with the isolated qutrit, this system has been simulated for different values of H_0 and g . Ch_1 is again found by integrating $\langle S^y \rangle$ over the sphere, this time for both qutrits as in Eq. (20). This phase diagram is plotted in Fig. 3(b). The phase diagram is very interesting for a number of reasons. First of all, it is interesting that while the uncoupled system only has a single transition where Ch_1 changes by 2, this system has a lot of possible transitions where Ch_1 can change by 1. For a fixed value of g between 0 and H_r , changing H_0 from

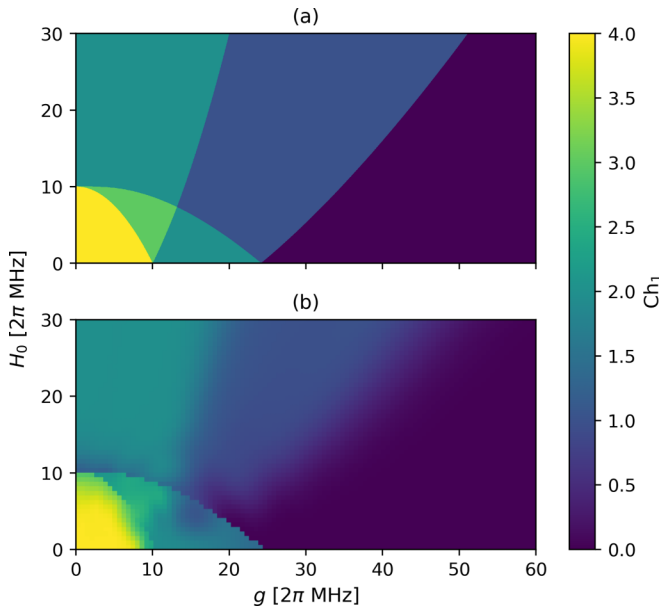


FIG. 3. (a) The theoretical phase diagram. Six different phases are present, with different values of Ch_1 . This was constructed by considering how many degeneracies are enclosed within the ground state manifold with $H_r = 10 \times 2\pi$ MHz. (b) Simulated phase diagram showing the value of Ch_1 , which was found by integrating $F_{\theta\phi}$, for different values of H_0 and g , with $H_r = 10 \times 2\pi$ MHz and $t_{\text{ramp}} = 0.5 \mu\text{s}$.

0 to $H_0 > H_r$ will still cause Ch_1 to change by 2, but in two steps. In Sec. III A, the change in Ch_1 by 2 could be interpreted as moving the single monopole with charge 2 from inside to outside the ground state manifold. This interpretation is no longer valid, given how it changes in two steps. Instead, one must interpret it as two distinct monopoles with charge 1. Likewise, for $H_0 = 0$, changing g allows for two different transitions, while for H_0 between 0 and H_r , four transitions occur.

The fact that the phases seem to “split” as g and H_0 increases is interesting in itself. The fact that there exist phases that are not driven purely by H_0 and g , but for specific values of these in combination, is in itself a rather remarkable result. This result is not possible in the spin-1/2 analog of the system, given that each particle only contributes with $Ch_1 = 1$ each, and only three phases are present [30]. This system therefore allows for completely new types of phases to occur that would not be possible for lower spin.

V. IMPLEMENTATION OF COUPLED QUTRIT SYSTEM

As an example of how a system of two coupled spin-1 systems, i.e., qutrits, could be implemented in a physical device, we look at the superconducting circuit proposed in Ref. [40], Sec. XIV. A lumped circuit element drawing of the system can be seen in Fig. 4. The system consists of three superconducting islands indicated by nodes in the figure. The islands are connected using Josephson junctions, capacitors, and inductors, while the bottom island is connected to the ground as a transmon [51]. The two effective coupled degrees of freedom can be seen as the dipoles fluctuating between the

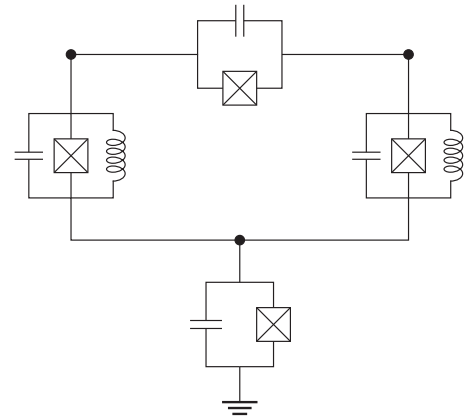


FIG. 4. A lumped-element circuit drawing of the proposed superconducting circuit implementing a coupled two-qutrit system with an effective Heisenberg XXZ interaction. Standard circuit notation is used, with the crossed boxes representing Josephson junction.

upper two islands, and between the lower island and equally to each upper island, respectively. The third degree of freedom is a combined fluctuation with respect to the ground and can thus be ignored. The ratio of the inductances and capacitances are chosen such that the two dipoles are in the transmon regime and can thus be truncated to the lowest three levels. The Hamiltonian from this circuit has the following form:

$$H = g (S_1^x S_2^x + S_1^y S_2^y) + J_z (S_1^z S_2^z) + \mathbf{H}_1 \cdot \mathbf{S}_1 + \mathbf{H}_2 \cdot \mathbf{S}_2 + H_0 S_1^z + \frac{J_{02}}{4} [(S_1^+ S_2^-)^2 + (S_1^- S_2^+)^2]. \quad (28)$$

A deeper explanation of how the Hamiltonian arises is beyond the scope of this paper; however, in the Appendix we describe briefly how the Hamiltonian of the system can be found, and how to modify it so that it is written in terms of spin-1 matrices. Further details can be found in Refs. [40] and [41], including a discussion of the parameters involved. Intuitively, the two effective degrees of freedom can be seen as the electrical field modes oscillating between the left and the right upper circuit nodes, and oscillating between the two upper circuit nodes (black dots in Fig. 4) and the bottom circuit node, respectively.

We note here that the J_{02} term is a nontrivial term that appears because of the nature of the superconducting circuit setup when it is driven in order to make the parameters configurable. We therefore need to ensure that this will not interfere with the topological properties and the phase diagram. Luckily, this turns out not to be the case, as we will discuss in the next section.

VI. EXPLORING THE LARGER PARAMETER SPACE

The new system is considerably more complicated than the one for a simple coupling, described in Sec. IV A. In the regime where $J_z \rightarrow 0$ and $J_{02} \rightarrow 0$, it reduces to the previously described system. It is quickly noted that this system also retains the $U(1)$ invariance, as can be seen by writing out

$$H(\theta, \phi) = e^{i\phi(S_1^z + S_2^z)} H(\theta, 0) e^{-i\phi(S_1^z + S_2^z)} \quad (29)$$

in matrix form.

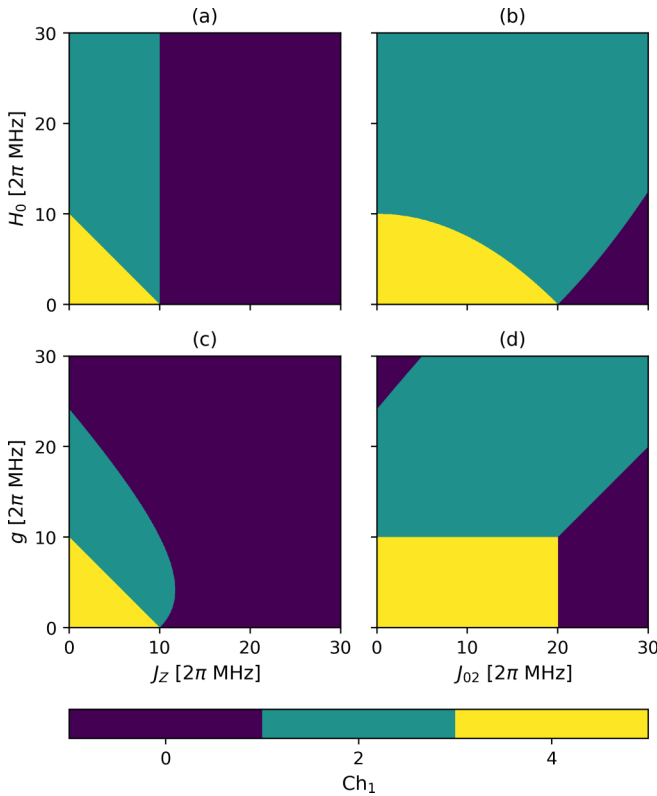


FIG. 5. Phase diagram for Ch_1 with $H_r = 10 \times 2\pi$ MHz for various types of coupling with all others absent. (a) H_0 and J_z . (b) H_0 and J_{02} . (c) g and J_z . (d) g and J_{02} .

In the case of the simple coupling in Sec. IV A, the interaction was controlled by S^x , S^y , S^z for both qutrits and $(S_1^x S_2^x + S_1^y S_2^y)$, giving a parameter space of dimension seven. Adding control of $S_1^z S_2^z$ and $[(S_1^+ S_2^-)^2 + (S_1^- S_2^+)^2]$ expands this to nine. Changing both the previous free variables, as well as the two new ones, would require four-dimensional phase diagrams. For convenience, we will only be plotting two-dimensional slices of this.

As before, we will be considering spherical manifolds with constant $|\mathbf{H}_1| = |\mathbf{H}_2| = H_r = 10 \times 2\pi$ MHz.

In the simple case of only two parameters, we can easily construct theoretical phase diagrams in a similar fashion to that of Sec. IV A. We will do so with the new coupling parameters. We will not provide in-depth derivation of the theoretical phase diagrams, since the procedure is identical to the one previously applied. That is, first reorient the axis to point in the \hat{z} direction, find ground state wave functions for each region, then locate the Weyl points. We have chosen to do this with a selection of the parameters, collected in Fig. 5.

Simulated diagrams can also be constructed by ramping $\theta(t)$ linearly and integrating $\langle S^y \rangle$ for each qutrit. This will not be presented. However, we note that all the theoretical values agree with simulations. The remainder of this section will be spent discussing the phase diagrams.

We first consider the effect of the J_z coupling. The resulting diagram is plotted in Fig. 5(a). As is evident in the figure, three phases are present, with transitions occurring at $H_0 + J_z = H_r$ and $J_z = H_r$. This phase diagram is quite different than the one for g -coupling, as the transitions are much simpler in this

regime. The fact that H_0 and J_z can both contribute equally to the transition where Ch_1 changes from 4 to 2, but only the coupling induces the transition where $Ch_1 \rightarrow 0$, is interesting. Alone, however, the diagram is not so illuminating.

Next, we focus on the effect of varying the parameters J_{02} and H_0 . This is presented in Fig. 5(b). It is worth noting that the phase diagram produced by this coupling is identical to the first phase of the one controlled by g -coupling, except with a scaling factor on the coupling parameter. To be exact, the z component of the Weyl point is

$$H_z = -\frac{H_0}{2} \pm \frac{1}{2} \sqrt{H_0^2 + J_{02}^2},$$

compared to

$$H_z = -\frac{H_0}{2} \pm \frac{1}{2} \sqrt{H_0^2 + 4g^2}$$

for g -controlled coupling.

The dynamics that are most common in spin chains are those governed by the coupling of the types $(S_1^x S_2^x + S_1^y S_2^y)$ and $(S_1^z S_2^z)$, controlled by g and J_z . Phase diagrams for the two couplings controlled by J_z and g are plotted in Fig. 5(c). As in the case values of J_z and H_0 , the first transition is controlled equally by the two parameters, while the second transition is of a more complex nature.

Finally, we focus on the effect of J_{02} and g as in Fig. 5(d). It can be seen that when $g < H_r$ and $J_{02} < 2H_r$, neither coupling is strong enough to change the topology, but that topological transitions occur when $g = H_r$ or $J_{02} = 2H_r$. The most interesting thing is perhaps that while a strong increase in either g or J_{02} will result in $Ch_1 \rightarrow 0$, we have $Ch_1 = 2$ when $J_{02} \approx g > H_r$, no matter their magnitude.

The phase diagrams presented here are very rich. This indicates that a relatively simple generalization of the case of two coupled spin-1/2 systems, as performed in Ref. [30], can give a much more varied set of topological phases as one tunes the parameters. We note that this comes at the expense of adding a single extra level to the superconducting circuits. Exploring these new phase diagrams in greater detail than what has been done here, by interpreting the phases and examining properties such as critical exponents of the topological transitions, for example, should be a venue for future work.

Furthermore, the lifetimes of higher states beyond the first two are typically only about a factor of two shorter. Compared to Ref. [29], where a ramping for a two-level system for 1 ms was performed, we expect that the three-level system can be explored in the same manner, with ramping times of the same order as explored in the simulations, i.e., at the level of around 0.5 ms. This may yield further insight into coupled higher-spin systems as a means of simulating topological phases in quantum systems.

VII. CONCLUSION AND OUTLOOK

In this paper, systems of interacting spins beyond the simple spin-1/2 system have been considered. Starting from a single spin-1 system, we introduced the theoretical groundwork in terms of spin-1 operators, Berry curvature, and the first Chern number in order to address the topological transitions that are possible for systems with higher spins.

Furthermore, we also connected these considerations to previous measurement protocols used to probe different topological phases, and how to induce transitions between different phases by changing system parameters. We then proceeded to add a second spin-1 system and studied the coupling of two such qutrits. This turns out to produce a considerably richer phase diagram compared to the case of coupled spin-1/2 systems. Finally, a system based on the platform of superconducting circuits was introduced that can be used to realize a set of coupled spin-1 systems, and suitably modified with drive lines in order to obtain control of different system parameters. The system was simulated for a large set of parameters and the ensuing dynamics was characterized. This allowed us to conclude that a lot of opportunities may lie in the experimental probing of higher spins for its topological properties.

Our analysis here did not take into account some issues that may arise in realizations with superconducting circuits. The issue of how noise may effect the phases and how to tune the driving or optimize the protocols in order to mitigate noise effects was left for future consideration.

Topological properties are of increasing interest in several fields of physics, since they allow for unique physical phenomena that typically goes beyond our basic intuitions, and the realization of topological phases in quantum simulators and in materials have become a very intensely pursued topic. In order to derive topological features of different physical systems, it is common to define mappings onto systems where topological features are easier to identify. Quite often, this will be to forms that are closely related to spins in magnetic fields. There have been some works along these lines (see, for instance, Refs. [30,52] and [36]). We therefore speculate that

the three-level systems coupled with J_{02} and J_Z terms can be mapped to a physical system in which the topological phases of Sec. VI become manifest. Furthermore, as was noted in Ref. [41], it is quite simple to imagine how to scale the present system of two qutrits to a larger chain of coupled qutrits using the superconducting circuit designs that lead to the Hamiltonian considered here. As is briefly mentioned at the end of Ref. [36], this could be used to implement the Haldane phase of an interacting spin-1 chain [53]. However, we note that some of the other platforms mentioned in the introduction that are currently in use for topological phase quantum simulations may also serve this purpose. Hence, the principle theoretical investigation started here with the coupling of two spin-1 systems could serve as a few-body precursor to the realization of many-body phases with manifest topological properties.

APPENDIX: SUPERCONDUCTING CIRCUITS

In Sec. V we introduced a Hamiltonian for a physical realization of a coupled three-level system, stemming from the circuit in Fig. 4. This Appendix briefly presents the full coupled Hamiltonian investigated in Ref. [41] and later in Ref. [40] and describes how to modify it to arrive at Eq. (28).

The circuit Hamiltonian can be derived by following the standard quantization procedure described in Refs. [40,54], see Refs. [40,41]. As described in the main text, the three nodes in the circuit couple in such a way that a change of basis can be performed to a coordinate system where a center-of-mass like degree of freedom can then be ignored. The result is the Hamiltonian of effectively two coupled qutrits, denoted by subscripts $i = 1$ and $i = 2$:

$$\begin{aligned}
H_{\text{full}} = & \Delta_{1,1}|1\rangle\langle 1|_1 + (\Delta_{1,1} + \Delta_{1,2})|2\rangle\langle 2|_1 + \Delta_{2,1}|1\rangle\langle 1|_2 + (\Delta_{2,1} + \Delta_{2,2})|2\rangle\langle 2|_2 \\
& + J_{01,01}(|0\rangle\langle 1|_1|1\rangle\langle 0|_2 + |1\rangle\langle 0|_1|0\rangle\langle 1|_2) + J_{01,12}(|0\rangle\langle 1|_1|2\rangle\langle 1|_2 + |1\rangle\langle 0|_1|1\rangle\langle 2|_2) \\
& + J_{12,01}(|1\rangle\langle 2|_1|1\rangle\langle 0|_2 + |2\rangle\langle 1|_1|0\rangle\langle 1|_2) + J_{12,12}(|1\rangle\langle 2|_1|2\rangle\langle 1|_2 + |2\rangle\langle 1|_1|1\rangle\langle 2|_2) \\
& + J_{02}(|0\rangle\langle 2|_1|2\rangle\langle 0|_2 + |2\rangle\langle 0|_1|0\rangle\langle 2|_2) + J_{ZZ}(D_{1,1}|1\rangle\langle 1|_1 + D_{1,2}|2\rangle\langle 2|_1)(D_{2,1}|1\rangle\langle 1|_2 + D_{2,2}|2\rangle\langle 2|_2), \quad (\text{A1})
\end{aligned}$$

using an outer product operator notation with the qutrits states denoted by 0, 1, and 2, respectively. The subscripts for Δ , D , and J are merely to distinguish them and to label which states they pertain to. We note here that we have performed the rotating wave approximation in order to arrive at the Hamiltonian [40]. The structure of the coupling is similar to XXZ -type Heisenberg couplings [55,56], but with some important modifications that are discussed below. These arise primarily from the driving terms required for full control of the system levels and the subsequent transformation to the rotating frame and diagonalization herein.

Here we will make the simplifying assumption that all parameters can be externally controlled independently of each other. This would require some additional drive lines for multimode driving or other techniques added onto the original model. The procedure for rewriting has been done by writing out the terms in matrix form with the Kronecker product, and comparing with how the spin matrices are given in the same basis. Since the matrices are rather large, we will not

write them out explicitly. By setting $J_{01,01} = J_{01,12} = J_{12,01} = J_{12,12} = g$, lines 3 and 4 can be written as

$$g(S_1^x S_2^x + S_1^y S_2^y),$$

i.e., $XX + YY$ -coupling that we considered in Sec. IV A.

It is possible to remove a constant on the diagonal of the Hamiltonian in order to set the lowest state at zero energy. Alternatively, we could throw away the middle $|1\rangle\langle 1|$ term and be left with $\Delta_{i,0}|0\rangle\langle 0|_i + (\Delta_{i,0} + \Delta_{i,2})|2\rangle\langle 2|_i$ for $i = 1, 2$ for both the terms acting directly on the qutrit and the coupling term. Setting $\Delta_{i,0} = -\Delta_{i,2}/2$, and similarly for the coupling term, gives rise to the terms

$$\Delta_1 S_1^z + \Delta_2 S_2^z + J_{ZZ}(S_1^z S_2^z).$$

Finally, the J_{02} term cannot immediately be written in terms of the S^x , S^y , or S^z spin-1 operators. It can, however, be written in terms of the ladder operators as

$$J_{02}[(S_1^+ S_2^-)^2 + (S_1^- S_2^+)^2]/4.$$

While not present in the presented circuit drawing (Fig. 4) for simplicity, adding terms giving control over S^x and S^y for both qutrits is a standard procedure. We refer to Ref. [40] for details. Adding these terms, we have an implementation of the required spin-1 operators added to the Hamiltonian.

In the end we have the Hamiltonian

$$H = g(S_1^x S_2^x + S_1^y S_2^y) + J_Z(S_1^z S_2^z) + \mathbf{H}_1 \cdot \mathbf{S}_1 + \mathbf{H}_2 \cdot \mathbf{S}_2 + H_0 S_1^z + \frac{J_{02}}{4} [(S_1^+ S_2^-)^2 + (S_1^- S_2^+)^2]. \quad (\text{A2})$$

This is Eq. (28) in the main text.

-
- [1] T. Kato, *J. Phys. Soc. Jpn.* **5**, 435 (1950).
- [2] M. V. Berry, *Proc. R. Soc. London A* **392**, 45 (1984).
- [3] D. J. Thouless, M. Kohmoto, M. P. Nightingale, and M. den Nijs, *Phys. Rev. Lett.* **49**, 405 (1982).
- [4] M. Kohmoto, *Ann. Phys.* **160**, 343 (1985).
- [5] X.-G. Wen, *Adv. Phys.* **44**, 405 (1995).
- [6] A. P. Schnyder, S. Ryu, A. Furusaki, and A. W. W. Ludwig, *Phys. Rev. B* **78**, 195125 (2008).
- [7] A. Kitaev, *AIP Conf. Proc.* **1134**, 22 (2009).
- [8] M. Z. Hasan and C. L. Kane, *Rev. Mod. Phys.* **82**, 3045 (2010).
- [9] X.-L. Qi and S.-C. Zhang, *Rev. Mod. Phys.* **83**, 1057 (2011).
- [10] C.-K. Chiu, J. C. Y. Teo, A. P. Schnyder, and S. Ryu, *Rev. Mod. Phys.* **88**, 035005 (2016).
- [11] C. Nayak, S. H. Simon, A. Stern, M. Freedman, and S. Das Sarma, *Rev. Mod. Phys.* **80**, 1083 (2008).
- [12] J. K. Pachos, *Introduction to Topological Quantum Computation* (Cambridge University Press, Cambridge, 2012).
- [13] B. A. Bernevig and T. L. Hughes, *Topological Insulators and Topological Superconductors* (Princeton University Press, Princeton, 2013).
- [14] R. P. Feynman, *Int. J. Theor. Phys.* **21**, 467 (1982).
- [15] I. M. Georgescu, S. Ashhab, and F. Nori, *Rev. Mod. Phys.* **86**, 153 (2014).
- [16] D.-W. Zhang, Y.-Q. Zhu, Y. Zhao, H. Yan, and S.-L. Zhu, *Adv. Phys.* **67**, 253 (2018).
- [17] N. R. Cooper, J. Dalibard, and I. B. Spielman, *Rev. Mod. Phys.* **91**, 015005 (2019).
- [18] C. S. Adams, J. D. Pritchard, and J. P. Shaffer, *J. Phys. B: At. Mol. Opt. Phys.* **53**, 012002 (2019).
- [19] A. Browaeys and T. Lahaye, *Nat. Phys.* **16**, 132 (2020).
- [20] R. Blatt and C. F. Roos, *Nat. Phys.* **8**, 277 (2012).
- [21] C. Monroe, W. C. Campbell, L.-M. Duan, Z.-X. Gong, A. V. Gorshkov, P. W. Hess, R. Islam, K. Kim, N. M. Linke, G. Pagano, P. Richerme, C. Senko, and N. Y. Yao, *Rev. Mod. Phys.* **93**, 025001 (2021).
- [22] L. Lu, J. D. Joannopoulos, and M. Soljačić, *Nat. Phys.* **12**, 626 (2016).
- [23] T. Ozawa, H. M. Price, A. Amo, N. Goldman, M. Hafezi, L. Lu, M. C. Rechtsman, D. Schuster, J. Simon, O. Zilberberg, and I. Carusotto, *Rev. Mod. Phys.* **91**, 015006 (2019).
- [24] Z.-L. Xiang, S. Ashhab, J. Q. You, and F. Nori, *Rev. Mod. Phys.* **85**, 623 (2013).
- [25] X. Gu, A. F. Kockum, A. Miranowicz, Y.-X. Liu, and F. Nori, *Phys. Rep.* **718-719**, 1 (2017).
- [26] P. Krantz, M. Kjaergaard, F. Yan, T. P. Orlando, S. Gustavsson, and W. D. Oliver, *Appl. Phys. Rev.* **6**, 021318 (2019).
- [27] M. Kjaergaard, M. E. Schwartz, J. Braumüller, P. Krantz, J. I.-J. Wang, S. Gustavsson, and W. D. Oliver, *Annu. Rev. Condens. Matter Phys.* **11**, 369 (2020).
- [28] A. Blais, A. L. Grimsmo, S. M. Girvin, and A. Wallraff, *Rev. Mod. Phys.* **93**, 025005 (2021).
- [29] M. D. Schroer, M. H. Kolodrubetz, W. F. Kindel, M. Sandberg, J. Gao, M. R. Vissers, D. P. Pappas, A. Polkovnikov, and K. W. Lehnert, *Phys. Rev. Lett.* **113**, 050402 (2014).
- [30] P. Roushan, C. Neill, Y. Chen *et al.*, *Nature (London)* **515**, 241 (2014).
- [31] M. Neeley, M. Ansmann, R. C. Bialczak, M. Hofheinz, E. Lucero, A. D. O'Connell, D. Sank, H. Wang, J. Wenner, A. N. Cleland, M. R. Geller, and J. M. Martinis, *Science* **325**, 722 (2009).
- [32] L. DiCarlo, J. M. Chow, J. M. Gambetta, L. S. Bishop, B. R. Johnson, D. Schuster, J. Majer, A. Blais, L. Frunzio, S. M. Girvin *et al.*, *Nature (London)* **460**, 240 (2009).
- [33] R. Bianchetti, S. Filipp, M. Baur, J. M. Fink, C. Lang, L. Steffen, M. Boissonneault, A. Blais, and A. Wallraff, *Phys. Rev. Lett.* **105**, 223601 (2010).
- [34] A. A. Abdumalikov, Jr., J. M. Fink, K. Juliusson, M. Pechal, S. Berger, A. Wallraff, and S. Filipp, *Nature (London)* **496**, 482 (2013).
- [35] M. J. Peterer, S. J. Bader, X. Jin, F. Yan, A. Kamal, T. J. Gudmundsen, P. J. Leek, T. P. Orlando, W. D. Oliver, and S. Gustavsson, *Phys. Rev. Lett.* **114**, 010501 (2015).
- [36] X. Tan, D.-W. Zhang, Q. Liu, G. Xue, H.-F. Yu, Y.-Q. Zhu, H. Yan, S.-L. Zhu, and Y. Yu, *Phys. Rev. Lett.* **120**, 130503 (2018).
- [37] T. Bækkegaard, L. B. Kristensen, N. J. Loft, C. K. Andersen, D. Petrosyan, and N. T. Zinner, *Sci. Rep.* **9**, 1 (2019).
- [38] N. J. S. Loft, M. Kjaergaard, L. B. Kristensen, C. K. Andersen, T. W. Larsen, S. Gustavsson, W. D. Oliver, and N. T. Zinner, *npj Quantum Inf.* **6**, 47 (2020).
- [39] K. Zhang, H. Li, P. Zhang, J. Yuan, J. Chen, W. Ren, Z. Wang, C. Song, D.-W. Wang, H. Wang, S. Zhu, G. S. Agarwal, and M. O. Scully, *Phys. Rev. Lett.* **128**, 190502 (2022).
- [40] S. E. Rasmussen, K. S. Christensen, S. P. Pedersen, L. B. Kristensen, T. Bækkegaard, N. J. S. Loft, and N. T. Zinner, *PRX Quantum* **2**, 040204 (2021).
- [41] T. Bækkegaard, Beyond the qubit: Exploiting higher-dimensional states in superconducting circuits and photonic systems, Ph.D. thesis, Aarhus Universitet, 2020.
- [42] J. R. Johansson, P. D. Nation, and F. Nori, *Comput. Phys. Commun.* **183**, 1760 (2012).
- [43] J. J. Sakurai and J. Napolitano, *Modern Quantum Mechanics*, 2nd ed. (Pearson, Upper Saddle River, 2012).
- [44] B. Simon, *Phys. Rev. Lett.* **51**, 2167 (1983).
- [45] R. Jackiw, *Int. J. Mod. Phys. A* **03**, 285 (1988).
- [46] D. J. Griffiths, *Introduction to Electrodynamics*, 4th ed. (Pearson Education, Upper Saddle River, 2012), p. 45.
- [47] V. Gritsev and A. Polkovnikov, *Proc. Natl. Acad. Sci.* **109**, 6457 (2012).

- [48] S. E. Rasmussen, K. S. Christensen, and N. T. Zinner, *Phys. Rev. B* **99**, 134508 (2019).
- [49] R. E. Barfknecht, S. E. Rasmussen, A. Foerster, and N. T. Zinner, *Phys. Rev. B* **99**, 144304 (2019).
- [50] S. E. Rasmussen and N. T. Zinner, *Phys. Rev. Res.* **2**, 033097 (2020).
- [51] J. Koch, T. M. Yu, J. Gambetta, A. A. Houck, D. I. Schuster, J. Majer, A. Blais, M. H. Devoret, S. M. Girvin, and R. J. Schoelkopf, *Phys. Rev. A* **76**, 042319 (2007).
- [52] G. Zhang, C. Li, and Z. Song, *Sci. Rep.* **7**, 8176 (2017).
- [53] F. D. M. Haldane, *Phys. Rev. Lett.* **50**, 1153 (1983).
- [54] U. Vool and M. Devoret, *Int. J. Circuit Theory Appl.* **45**, 897 (2017).
- [55] N. J. S. Loft, L. B. Kristensen, C. K. Andersen, and N. T. Zinner, [arXiv:1802.04292](https://arxiv.org/abs/1802.04292).
- [56] K. S. Christensen, S. E. Rasmussen, D. Petrosyan, and N. T. Zinner, *Phys. Rev. Res.* **2**, 013004 (2020).